Fluid Dynamics &
Materials Processing

Tech Science Press

http://doi.org/10.32604/fdmp.2026.080516

ARTICLE

A Coupled PBM-FEM-SPH Investigation of Air-Decked Charge Structures for Improved Fragmentation and Flyrock Control in Bench Blasting

Zuoming Yin[1,2,*], Qiang Zhao[1], Feng Xie[1], Jingjiu Bi[1], Jianlong Wang[1], Shupeng Zhang[1], Haonan Wang[1] and Xiaolong Li[1]

[1]North Blasting Technology Co., Ltd., Beijing, China
[2]Key Laboratory of Ministry of Education for Efficient Mining and Safety of Metal Mines, University of Science and Technology Beijing, Beijing, China
*Corresponding Author: Zuoming Yin. Email: zuomingyin@163.com

Received: 11 February 2026; Accepted: 12 May 2026; Published: 30 June 2026

ABSTRACT: Optimizing the utilization of explosive detonation energy through bench blasting is central to improving both the efficiency and safety of open-pit mining operations. However, conventional blasting geometries often produce a non-uniform energy distribution, with excessive toe burden at the bench base and insufficient crest burden near the slope top, conditions that can significantly increase the risk of flyrock. This study proposes an air-decked charge configuration to mitigate these imbalances and enhance blast performance. A coupled numerical framework integrating the Particle Blast Method, Finite Element Method, and Smoothed Particle Hydrodynamics is employed, complemented by high-speed photographic field monitoring, to examine rock fragmentation behavior and the evolution of fragment velocities under air-decked loading conditions. The results show that air-decked configurations promote a more uniform borehole pressure distribution and markedly reduce the initial ejection velocity of rock fragments along the slope, effectively suppressing flyrock generation. In particular, for top air-deck arrangements, an optimal air-deck-to-charge length ratio in the range of 27% to 36% is identified, achieving a favorable balance between fragmentation efficiency and hazard control.

KEYWORDS: Open-pit mine; air deck charge; fly rock; particle blast method (PBM)

1 Introduction

Optimizing the utilization of explosive detonation energy through bench blasting is fundamental to enhancing the efficiency of open-pit mining operations [1,2]. Despite its widespread application, the effective utilization of explosive energy typically remains within the 20%–30% range; the remaining energy dissipates as unwanted ground vibrations, near-field rock over-crushing, and hazardous fly rock [3]. To mitigate these adverse effects and improve energy partition, researchers have extensively investigated the shockwave dynamics associated with air-decked charge structures [4]. Engineering practice and experimental studies have confirmed that air-decked configurations can enhance energy utilization, optimize rock fragmentation, and effectively regulate rock ejection trajectories [5].

In large-scale Chinese open-pit mines, bench heights typically range from 12 to 15 m. Increasing these heights to reduce stripping costs while accommodating large-scale equipment remains a formidable challenge in deep-hole blasting technology [6–8]. During field operations, the nonlinear distribution of the burden along the borehole depth—exacerbated by free-face effects—frequently triggers hazardous fly

rock. Addressing this phenomenon requires a more balanced borehole pressure distribution and improved fragmentation quality, for which air-decked charge structures offer a viable solution [3,9].

Conventional blasting methods often lead to excessive pulverization in the immediate vicinity of the borehole, which consumes a disproportionate amount of explosive energy [10]. To reduce such losses, air gaps are strategically incorporated along the charge axis to moderate peak pressures [11]. Fang et al. [12] conducted an experimental investigation using a modified split Hopkinson pressure bar system to characterize the dynamic mechanical behavior and energy dissipation of deep rock subjected to coupled impact loading and hydrostatic pre-stress. Their study revealed the significant influence of fracture energy absorption of the rock material. Ding et al. [13] integrated fractal damage theory with energy release rate analysis to compare the performance of coupled and decoupled charges. Furthermore, Zuo et al. [14] demonstrated an inverse correlation between decoupling coefficients and the extent of ore damage. Mechanistic insights have also been provided by Ding et al. [15], who employed dynamic strain measurements and high-speed photography to elucidate fracture mechanisms, and Zhu et al. [16], who derived stabilized borehole pressure formulas based on shockwave theory. Additionally, Wang and Xiang et al. [17] utilized LightGBM machine learning models to achieve promising results in predicting fly rock distances in lead-zinc mines.

Despite these advancements, few studies have addressed the real-time rock movement and damage evolution across distinct bench layers during the blasting process. In numerical modeling, LS-DYNA is the standard for simulating nonlinear problems involving explosive detonation in multiphase media (gas, fluid, and solid) [18]. Mitelman et al. [19] integrated the Finite Element Method (FEM) and Discrete Element Method (DEM) with a coupled Eulerian-Lagrangian solver to simulate blast-induced shockwaves adhering to Rankine-Hugoniot relations. Recent developments in the Particle Blast Method (PBM) and Smoothed Particle Hydrodynamics (SPH) now enable high-fidelity modeling of borehole detonation processes and gas behavior under extreme conditions [20,21].

The integration of machine learning with multiphysics blasting models—as exemplified by recent LightGBM applications [18]—opens new avenues for predictive fly rock management. This study seeks to bridge the gap between mechanistic modeling and empirical data by employing a coupled PBM-FEM-SPH numerical approach validated through field monitoring. By systematically analyzing the influence of air-deck configurations on fly rock suppression and fragmentation, this research provides theoretical insights and empirical support for advancing safe and efficient open-pit mining technologies.

2 Analysis of Detonation Product Flow in the Upper Air-Decked Charge Structure

2.1 Coupling Strategy of PBM-FEM-SPH

The three numerical domains are coupled through a combination of particle-particle and tied-interface contacts, all executed under the same explicit time-stepping scheme [22,23].

(a) PBM–SPH coupling.

A penalty-based particle-to-particle contact algorithm is employed. When a PBM particle penetrates the support domain of an SPH particle, a contact spring is inserted between the two. The contact force is proportional to the penetration depth and a contact stiffness that is scaled with the bulk modulus of the explosive products. This force resists further penetration and transfers mechanical work from the expanding detonation products to the SPH particles, thereby coupling the explosive energy to the rock.

(b) SPH–FEM coupling.

The SPH particle cloud is attached to the adjacent FEM surface by a tied-interface contact. Each SPH particle that lies within a user-specified distance of the FEM surface is constrained to move with the local nodal velocity of the FEM mesh. This constraint is enforced by a penalty method, and the reaction forces are assembled into the global system, ensuring continuity of displacement and momentum across the interface. The tied interface also transmits stress waves from the SPH domain into the FEM domain.

(c) Transition from continuum (FEM) to particle (SPH) representation.

In the immediate neighbourhood of the borehole, where damage is expected to be severe, the initial mesh is populated with SPH particles from the start; no dynamic conversion is required in the primary damage zone. However, to allow progressive fragmentation if needed, a conversion criterion is implemented: any FEM element in which the effective plastic strain exceeds a threshold value 0.15 is deleted and replaced by a set of SPH particles. The mass, momentum, and internal energy of the deleted element are mapped conservatively onto the new particles, which thereupon interact with the existing SPH domain through contact.

(d) Time integration and stability.

All three subdomains are advanced in time using the central-difference explicit integrator. The global time step is taken as

$$\begin{aligned} &\Delta t = C_{CFL} \cdot \min(\Delta t_{FEM}, \Delta t_{SPH}) \\ &C_{CFL} = 0.67 \end{aligned} \tag{1}$$

where Δt_{FEM} is the smallest element-based Courant limit and Δt_{SPH} is given by

$$\Delta t_{SPH} = \min_i \left(\frac{h_i}{ci + |v_i|}\right) \tag{2}$$

with c_i the local sound speed. Contact stiffnesses are scaled automatically by the solver, but we found that a contact stiffness scale factor of [0, 1] gave satisfactory stability without excessive energy dissipation.

2.2 Calibration of RHT Constitutive Model Parameters for Alaskite

The Riedel-Hiermaier-Thoma (RHT) constitutive model is highly effective for simulating rock blasting due to its ability to account for pressure-dependent strength, strain hardening, and rate effects. Seven fundamental parameters for the Alaskite rock mass were determined through static mechanical testing: density ρ, shear modulus, compressive strength σ_c, uniaxial tensile strength σ_t, initial porosity, and the ratios of tensile and shear strength to compressive strength. The physical-mechanical properties of the Alaskite, obtained from slope-cut field samples, are summarized in Table 1.

Table 1: Physical-mechanical parameters of Alaskite.

Rock Type	Density ρ (g/cm^3)	P-Wave Velocity Vp (m/s)	Tensile Strength σ_t (MPa)	Compressive Strength σ_c (MPa)	Elastic Modulus E (GPa)	Poisson's Ratio μ	Cohesion C (MPa)	Friction Angle φ (°)
Alaskite	2950	3170	7.84	159.65	24.16	0.238	21.52	53.77

Six parameters govern strain rate effects, with partial parameters predefined by the model. Reference compressive $\dot{\varepsilon}_0^{\mathrm{c}} = 3.0 \times 10^{-8}$ ms^{-1}. Reference tensile strain rates $\dot{\varepsilon}_0^{\mathrm{t}} = 3.0 \times 10^{-9}$ ms^{-1}. Failure compressive

$\dot{\varepsilon}^{c} = 3.0 \times 10^{22}$ ms^{-1}. Failure tensile strain rates $\dot{\varepsilon}^{t} = 3.0 \times 10^{22}$ ms^{-1}. Strain rate of compressive and tensile exponents calculated as:

$$\begin{aligned} \beta_c &= \tfrac{4}{20+3f_c} \\ \beta_t &= \tfrac{2}{20+f_c} \end{aligned} \tag{3}$$

Hugoniot polynomial coefficients are A_1, A_2 and A_3. EOS parameters are B_0, B_1, T_1 and T_2, which satisfy:

$$\begin{aligned} A_1 &= \rho_0 c_0^2 \\ A_2 &= \rho_0 c_0^2 (2s-1) \\ A_3 &= \rho_0 c_0^2 \left(3s^2 - 4s + 1\right) \\ T_1 &= \rho_0 c_0^2 \\ B_0 &= B_1 = 2s - 1 \\ T_2 &= 0 \end{aligned} \tag{4}$$

where A_1, A_2 and A_3 are the Hugoniot polynomial coefficients. c_0 denotes the bulk sound speed of the material at zero pressure. S is an empirical coefficient with lithology-dependent values as provided in Meyers' seminal work (Meyers, 1994): Marble: s = 0.95; Granite: s = 1.2. The damage parameters D1 and D2 were determined based on dynamic triaxial experimental data of the Alaskite in the study area, with reference to typical values for similar hard rocks in the literature. The damage parameters D1 and D2 are initially set to 0.04 and 1 respectively. The minimum residual strain at failure $\varepsilon_p^{\mathrm{m}}$ is related to damage and is taken as 0.01. The strength-related parameter P_{crush} represents the elastic limit pressure of the material, which can be obtained from $P_{\mathrm{crush}} = 2f_c/3$. The tensile-compressive meridian ratio parameter Q and the Lode angle correlation coefficient B can be fitted to obtain Q = 0.68 and B = 0.05. The failure surface parameters A and N can be obtained from the failure surface expression when $3P_0^* \geq F_{\mathrm{r}}$. When the material is under quasi-static loading conditions, F_r is taken as 1. Therefore, when $3P_0^* \geq F_r$, the definition formula of the failure surface curve is as follows:

$$\sigma_f^*\left(P_0^*, F_r\right) = \begin{cases} A\left(P_0^* - F_r/3 + (A/F_r)^{-1/N}\right)^N & 3P_0^* \geq F_r \\ F_r F_s^*/Q_1 + 3P_0^*\left(1 - F_s^*/Q_1\right) & F_r > 3P_0^* \geq 0 \\ F_r F_s^*/Q_1 - 3P_0^*\left(1/Q_2 - F_s^*/\left(F_t^* Q_1\right)\right) & 0 > 3P_0^* \geq 3P_t^* \\ 0 & 3P_t^* > 3P_0^* \end{cases} \tag{5}$$

$$\sigma_f^* = A\left(P_0^* - 1/3 + (A)^{-1/N}\right)^N \tag{6}$$

$$P_0{}^* = (\sigma_1 + 2\sigma_3)/3f_{\mathrm{c}} \tag{7}$$

$$\sigma_{\mathrm{f}}^* = \sigma_1 - \sigma_3/f_{\mathrm{c}} \tag{8}$$

The triaxial confining pressure relationship is estimated from the uniaxial compressive strength based on the Hoek-Brown strength criterion. The pore pressure at compaction P_{comp} is 6 GPa. The porosity index n_p is 3. The shear modulus reduction coefficient ξ is 0.5. The remaining four parameters are determined through debugging and set as follows: the compression yield surface parameter g_c^* is 0.53, the tension

yield surface parameter g_t^* is 0.7, the residual stress strength parameter A_f is 1.6, and the residual stress strength index n_f is 0.61. Some scholars have determined the order of influence of each factor through range analysis, obtaining that the compression yield surface parameter g_c^* has the greatest impact on the numerical simulation results, while the minimum effective strain $\varepsilon_p^{\mathrm{m}}$ has the least impact. System parameters: the unit system parameter onempa is set to 0; Gruneisen gamma is set to 0; the erosion plastic strain is set to 2.0.

2.3 Experimental Validation of RHT Constitutive Model Parameters

Experimental specimens with dimensions of diameter D = 50 mm and height H = 100 mm were prepared. A borehole of diameter φ = 3 mm and depth L = 70 mm was drilled axially. The charge consisted of lead azide (150 mg) packed in a thin plastic tube (2 mm diameter, 50 mm charge height), sealed at both ends with modeling clay (20 mm plug length). Detonation was initiated by high-voltage electric discharge via a 0.5 mm enamel-coated wire positioned at the borehole base. The borehole was stemmed with sand particles bonded by cyanoacrylate adhesive. Post-blast failure patterns exhibited close agreement with numerical simulations.

Cylindrical specimens (φ50 mm × φ100 mm) were prepared for the experimental investigation. A central axial borehole, with a diameter of 3 mm and a depth of 70 mm, was precisely drilled into each specimen. The explosive charge, comprising 150 mg of lead azide, was encapsulated within a thin plastic tube (φ2 mm, 50 mm length) and sealed at both ends using 20-mm modeling clay plugs. Detonation was triggered via high-voltage electrical discharge through a 0.5-mm enamel-coated wire positioned at the base of the borehole. Stemming was achieved using sand particles consolidated with a cyanoacrylate adhesive. The observed post-blast fracture morphologies showed excellent correlation with the results of the numerical simulations, thereby validating the modeling approach and the selected constitutive parameters.

The numerical model simulates a bottom-hole initiation configuration. Upon initiation, the detonation wave propagates spherically from the point of origin, while the resulting shock wave advances unidirectionally along the borehole axis. Due to the influence of flow deflection angles, a portion of these shock waves converges near the initiation site. This constructive interference generates a localized high-pressure zone where peak pressures exceed the characteristic detonation pressure, leading to concentrated material damage, as illustrated in Fig. 1a.

As the detonation front advances upward, the explosive column undergoes bi-directional flow dynamics during the expansion phase. Consequently, X-shaped shock wave intersections develop both ahead of and behind the reaction zone, driven by oblique shock reflections and flow deflection angles within the confined borehole geometry. Upon reaching the air-deck section, the detonation front transitions into a medium with significantly lower impedance. In the absence of further chemical energy release, the transition from the dense explosive column to the air gap creates a configuration functionally analogous to a Laval nozzle. The rapid expansion of high-pressure detonation products into the air-deck section generates an intensified damage zone, the radial extent of which frequently exceeds the damage observed along the primary explosive column.

The subsequent interaction at the interface between the air deck and the stemming material involves complex reflection and transmission phenomena. Due to the high porosity and low acoustic impedance of the loose stemming material, a substantial fraction of the incident shock energy is dissipated through irreversible compressive work. Simultaneously, the convergence of waves propagating opposite to the primary detonation front (tail-end waves) and those reflected from the stemming interface creates a

secondary high-pressure zone. However, owing to the significant energy dissipation during stemming compression, the peak pressure in this secondary zone remains lower than the peak pressure recorded at the borehole base.

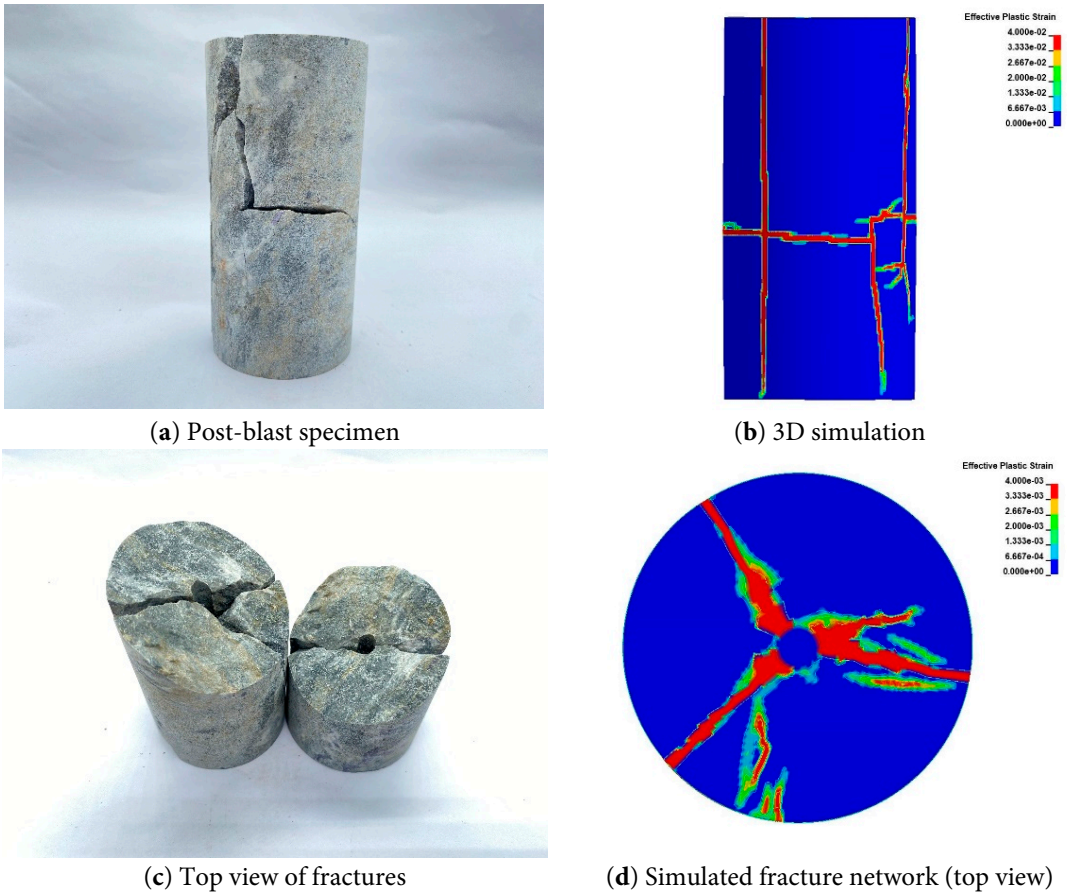

(**a**) Post-blast specimen (**b**) 3D simulation

(**c**) Top view of fractures (**d**) Simulated fracture network (top view)

Figure 1: Experimental and numerical comparison of Alaskite blasting (**a**–**d**).

2.4 Development of the PBM-FEM-SPH Coupled Model

Due to the difficulty in obtaining the borehole wall load of air-decked charges through experimental methods, a coupled Particle Blast Method, Smoothed Particle Hydrodynamics, and Finite Element Method (PBM-SPH-FEM) approach was employed. Both the FEM elements and SPH particles were assigned the RHT constitutive model. The stemming material was modeled as SPH particles, the rock medium as FEM elements, and the explosives and air inside the borehole as PBM particles. This study investigates the interaction between explosive detonation and the air inside the borehole, the flow characteristics of the detonation gases, and the dynamic response of the rock. The stress cloud diagrams from the numerical simulation of upper air-decked charge blasting at different time steps are shown in Fig. 2.

It is generally accepted that the mechanical response induced in rock by explosive blasting can be divided into two consecutive stages: the dynamic loading stage and the quasi-static loading stage. The former, acting as a stress wave or shock wave, can rapidly reach a relatively high peak value at the initial moment of blasting. The stress wave applied to the borehole wall crushes the surrounding rock and decays sharply over time. Once the stress wave has excited vibrations in the rock around the borehole and initiated

radial cracks, a longer-lasting quasi-static load follows. The role of the stress wave is to generate initial cracks, while the explosion gas pressure contributes to crack propagation.

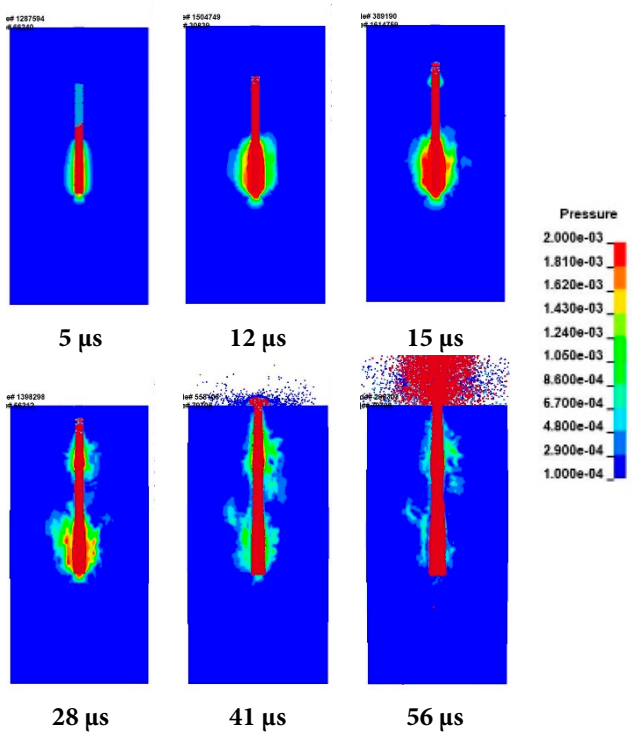

Figure 2: Numerical simulation results of upper air-decked charge blasting.

As can be seen from Fig. 2, from detonation initiation to the moment the shock wave reaches the air-decked section after detonation completion, the stress distribution in the medium surrounding the charged section resembles a water droplet shape. The stress attenuates after the detonation wave transforms into a shock wave and performs work by compressing the air. At 28 μs, the detonation products reach the stemming at the top of the hole, are reflected, and then propagate toward the hole bottom. At 41 μs, the stemming at the top of the hole is ejected, causing the pressure inside the hole to decay instantaneously. By 56 μs, the pressure inside the hole has essentially decayed to zero. The presence of the air deck significantly increases the flow time of the detonation products and the propagation time of the shock wave within the hole, thereby extending the action duration. To clarify the fragmentation characteristics near the air-decked charge blasting zone, the following discusses the evolution of blasting load over time, as shown in Fig. 3.

By monitoring pressure changes at different locations along the borehole wall, the time-history curves of borehole wall pressure at various positions for upper air-decked charge blasting were obtained. The charged section reached its peak pressure of 390 MPa at 15 μs, with the peak point located in the middle-lower part of the charged section. The air-decked section reached its peak pressure of 173 MPa at 34 μs, with the peak point situated in the upper region near the stemming area.

As shown in Fig. 3, unlike the fully charged column structure, the borehole wall pressure in the charged section does not remain stably at the peak pressure until the completion of continuous detonation. Instead, attenuation begins near the air deck section and continues until the detonation ends and the stress wave propagates through the air deck section. For monitoring points 3 and 4 in the air-decked section, which are closer to the charged section, the peak pressure is lower than that at points farther from the charged

section. This is mainly because the shock wave attenuates rapidly in the air deck section. In the air-decked charge structure, the pressure on the borehole wall in the uncharged air deck section is primarily generated by the expansion work of the detonation gases.

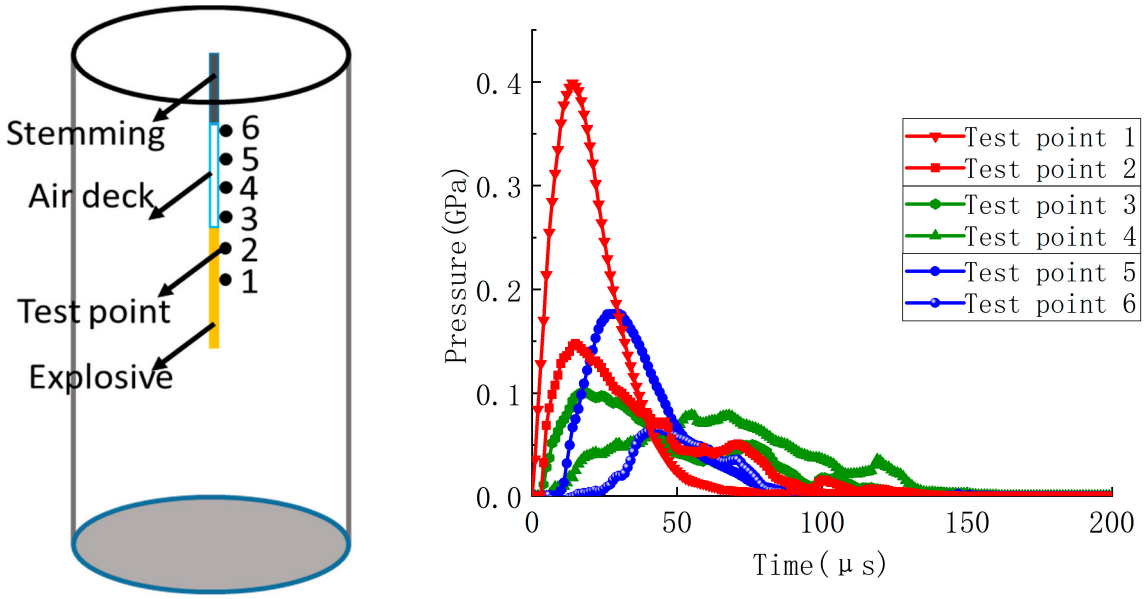

Figure 3: Time-history curves of borehole wall pressure at different locations for upper air-decked charge blasting.

The pressure-reducing effect of the air-decked charge structure on the detonation pressure inside the borehole can be analyzed by monitoring the pressure time-history curves of the numerical simulation units on the borehole wall. When a spherical charge is initiated, the detonation wave spreads outward symmetrically from the initiation point. In deep-hole blasting with column charges, detonation typically propagates in a water-droplet shape along the charge direction. It has found that in an infinite medium, the curvature radius of the wave front during the initial detonation stage is related to the charge length. The longer the charge length, the larger the curvature radius, with the two increasing linearly in direct proportion. For most condensed explosives, the maximum curvature radius is generally 2 to 3.5 times the charge diameter. This observation aligns with the load distribution on the borehole wall units monitored in Fig. 3. Therefore, influenced by the detonation wave curvature radius and the air deck, the air deck also affects the peak pressure in the charged section.

As shown in Fig. 4, the peak average pressure on the borehole wall in the charged section is 295 MPa, with an explosive load duration of 105 microseconds, a pressure rise time of 15 μs, and a pressure decay time of 90 μs. In the air-decked section, the peak average pressure on the borehole wall is 83 MPa, with an explosive load duration of 135 microseconds, a pressure rise time of 30 μs, and a pressure decay time of 105 μs. Compared to the charged section, the pressure rise time in the air-decked section is doubled, while the average pressure is reduced by 70%. In comparison to a fully charged column structure, the average pressure in the charged section is reduced by 17.8%, the explosive load duration is increased by 40%, and the pressure decay time is increased by 91%. Additionally, the quasi-static action time of the detonation products is significantly extended, which is more conducive to crack propagation. The failure of rock media exhibits a strong strain rate effect. Therefore, under explosive loads with different loading rates, the morphology of blast-induced cracks inevitably undergoes significant changes. The final damage morphology of the rock specimen after blasting is depicted in Fig. 5.

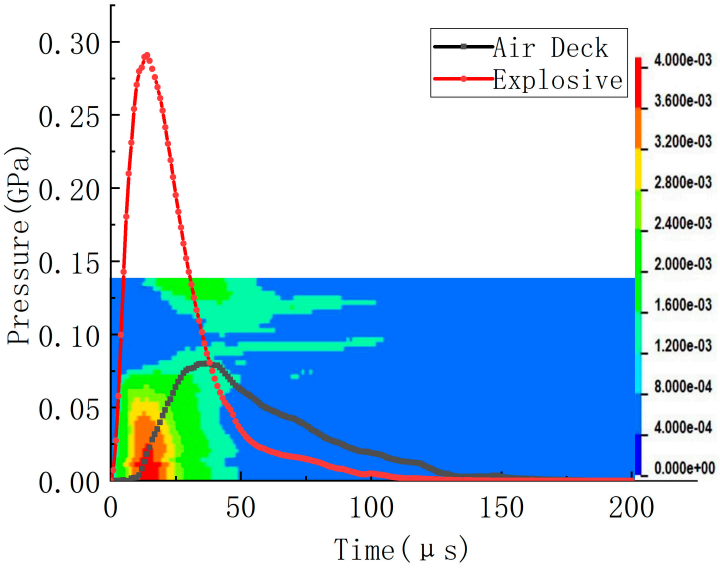

Figure 4: Average pressure contour on the borehole wall for upper air-decked charge blasting.

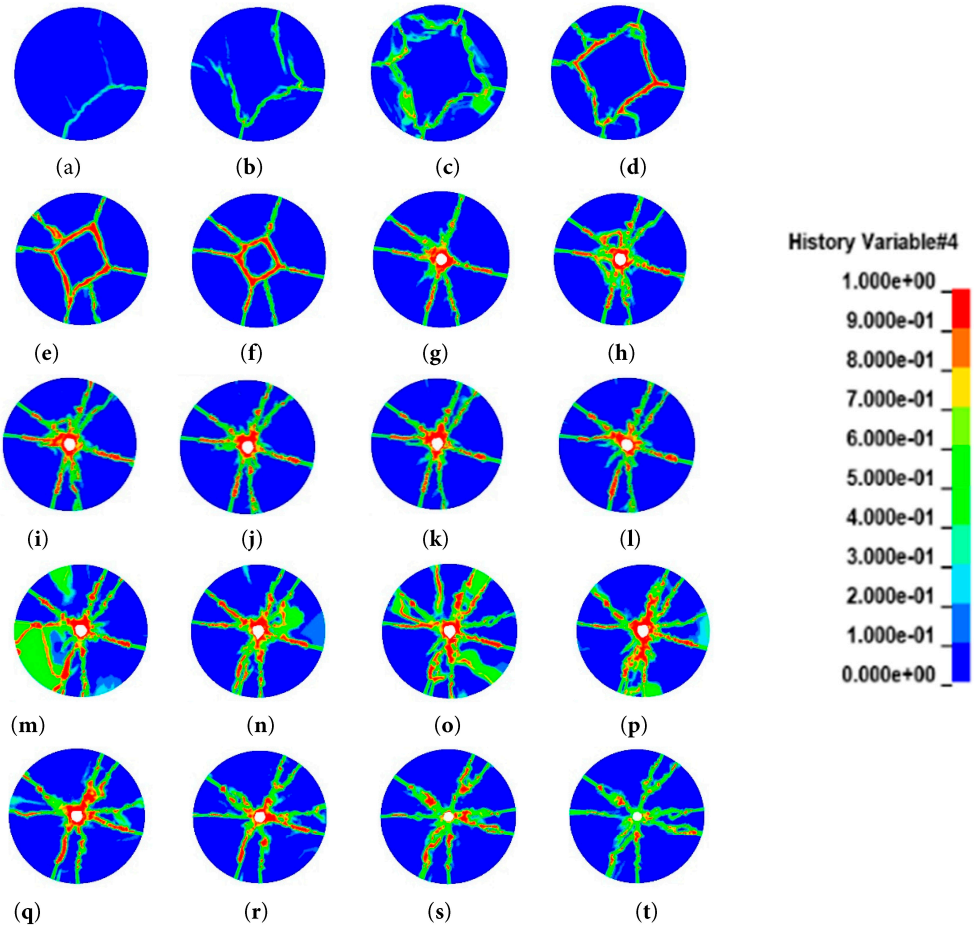

Figure 5: Damage pattern of upper air-decked charge blasting (**a**–**t**).

Fig. 5 shows the numerical simulation damage images for different segments: (Fig. 5a–f) the hole bottom segment (70–100 mm from the collar), (Fig. 5g–j) the charged segment (50–70 mm from the collar), (Fig. 5k–n) the air-decked segment (30–50 mm from the collar), and (Fig. 5o–t) the stemming segment (0–30 mm from the collar).

In the hole bottom segment, visible cracks consist of one main crack and two secondary cracks. Closer to the bottom charge column, the cracks exhibit a radially scattered distribution, increasing in number to six. At the bottom of the charged segment, six cracks are visible. As the detonation of the column charge concludes, the number of cracks in the air-decked segment does not increase but gradually decreases to seven. From images (m, n), it can be observed that near the collar stemming segment, transverse shear damage forms a shadowed area. In the stemming segment of the specimen, seven visible cracks extend directly to the collar.

3 Numerical Analysis Results

3.1 Establishment of the PBM-SPH-FEM Model

The Particle Blast Method (PBM) accounts for the co-volume effect, providing a superior thermodynamic characterization of detonation products under extreme pressure and temperature conditions. This allows for a more high-fidelity representation of the expansion behavior of gases within the borehole compared to conventional methods. Given that borehole wall loading in deep-hole blasting is inherently difficult to quantify experimentally, a multiphysics coupling approach—integrating PBM, Smoothed Particle Hydrodynamics (SPH), and the Finite Element Method (FEM)—was adopted.

In this hybrid framework, the in-hole explosive charge is represented by PBM particles to accurately capture the gas-solid interaction and the pressure pulse transmitted to the borehole walls. To accommodate the large deformations and flow behavior of the material during the blast, the stemming material is modeled using SPH particles. The surrounding rock mass is discretized using FEM elements to efficiently capture wave propagation and fracture evolution. Both the SPH (stemming) and FEM (rock) domains utilize the Riedel Hiermaier Thoma (RHT) constitutive model, which is well-suited for simulating pressure-dependent strength, strain hardening, and damage in geological materials. The comprehensive configuration and spatial discretization of the coupled PBM-SPH-FEM model are illustrated in Fig. 6.

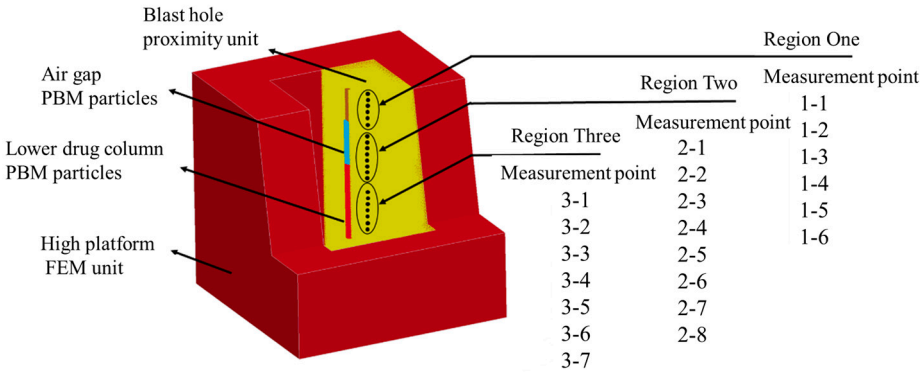

Figure 6: Schematic diagram of the numerical model depicting the air deck length parameter in a vertical borehole.

To evaluate the influence of air-decking on the duration of borehole pressure and the resulting rock movement, monitoring points were strategically positioned along the bench slope profile from the crest to the toe, as illustrated in Fig. 6. These surface monitoring points were categorized into three distinct zones

based on their relative position to the borehole: Zone 1: Located on the upper slope surface corresponding to the stemming section. Zone 2: Situated on the upper slope region characterized by a smaller burden, where the risk of fly rock is most acute. Zone 3: Located on the lower slope region where the burden is significantly larger. Given the reduced burden at the bench crest in deep-hole blasting, a top air-decked charge structure was adopted to optimize energy distribution. A parametric study was subsequently conducted involving seven numerical cases. These included a baseline full-column charge and six air-deck configurations with length ratios (μ_j), defined as air-deck length to total charge length of 0.09, 0.18, 0.27, 0.36, 0.45, and 0.55. These simulations aim to identify the correlation between the air-deck ratio and the mitigation of hazardous blasting effects.

3.2 Analysis of Blasting Fragmentation Effects with Different Air Deck Lengths

The Smoothed Particle Hydrodynamics (SPH) particles are governed by a kernel-based potential function. However, under conditions of extreme displacement and large-scale deformation, the method is susceptible to numerical divergence and the accumulation of computational errors. In rock damage simulations, this can lead to an unphysical expansion of the damage zone over time. As deformation surpasses the threshold of constitutive applicability for the original potential function, the reliability of the particle interactions diminishes. To maintain physical accuracy and ensure data integrity, the statistical evaluation of the rock mass damage extent was restricted to a temporal window of three times the characteristic detonation duration.

In open-pit mining, the quality of rock fragmentation is a critical performance indicator for evaluating the efficacy of charge structures. Based on the numerical results, a comparative analysis was performed to examine the damage patterns associated with varying air-deck length ratios (μ_j). For the full-column charge configuration, the rock mass in the upper region—characterized by the smallest burden—underwent excessive comminution and over-crushing. This phenomenon indicates a localized over-concentration of energy, which reduces overall blasting efficiency and contributes to fly rock hazards (Fig. 7). When the air-deck length ratio was introduced at μ_j = 0.09, the resulting attenuation of the peak borehole pressure led to a detectable decrease in the size of the comminution zone within the upper section. At the optimal ratio of μ_j = 0.27, the peak pressure was significantly moderated. In this case, the sustained quasi-static pressure from the expanding detonation products was sufficient to achieve the desired fragmentation at the slope crest while notably minimizing the volume of over-crushed material (Fig. 7). However, as the ratio increased to μ_j = 0.36, the reduction in explosive energy density became the limiting factor. At this threshold, the fragmentation quality began to degrade, evidenced by the appearance of coarse, oversized fragments at the slope crest. This suggests that while air-decking is effective for hazard mitigation, a ratio exceeding 0.36 may compromise the required fragmentation size distribution for downstream excavation and processing.

As the air-deck length ratio was increased to 0.36, the resulting attenuation of borehole pressure proved insufficient to satisfy the fragmentation requirements for the upper burden. This led to a significant increase in coarse fragmentation and the emergence of oversized boulders. To systematically evaluate the influence of the air-deck configuration on breakage patterns, twelve horizontal cross-sections were analyzed at regular intervals from the bench crest to the toe. The air deck serves a dual purpose: it reduces the total charge mass and lowers the peak detonation pressure, while simultaneously extending the duration of the quasi-static gas action—a phenomenon particularly critical near the free face of the slope crest where the burden is minimal. A comparative assessment with Fig. 4 reveals that while a full-column charge results in undesirable over-comminution in the upper small-burden zone, an air-deck ratio exceeding 0.36 results

in inadequate rock breakage due to insufficient energy density. This transition from over-pulverization to inadequate fragmentation underscores the sensitivity of the rock mass response to the charge structure. Based on these numerical findings and the observed fragmentation distribution, as shown in Fig. 8, an optimal air-deck length ratio (μ_j) ranging from 27% to 36% is recommended for top-air-deck configurations in vertical boreholes. This range provides the necessary balance between peak pressure moderation and the sustained energy required for efficient fragmentation.

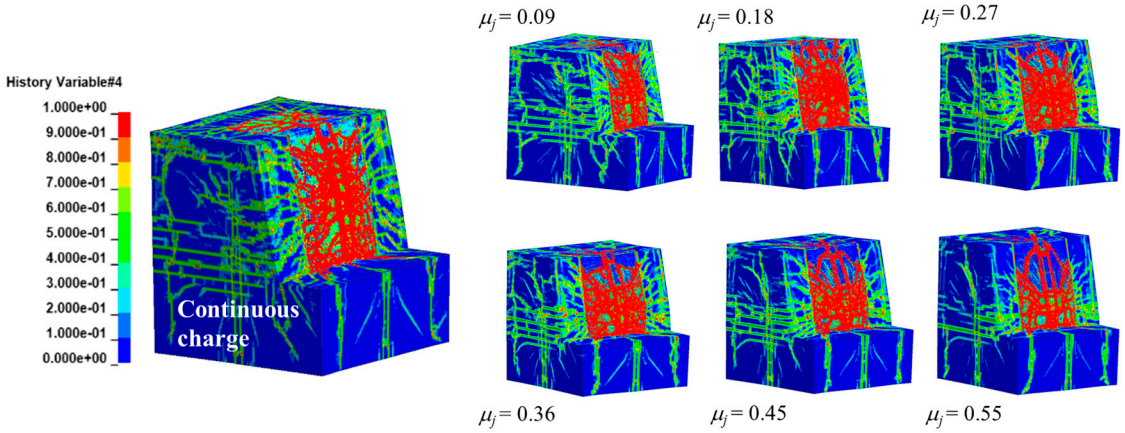

Figure 7: Three-dimensional numerical simulation of charge loading in cavities with different length ratios.

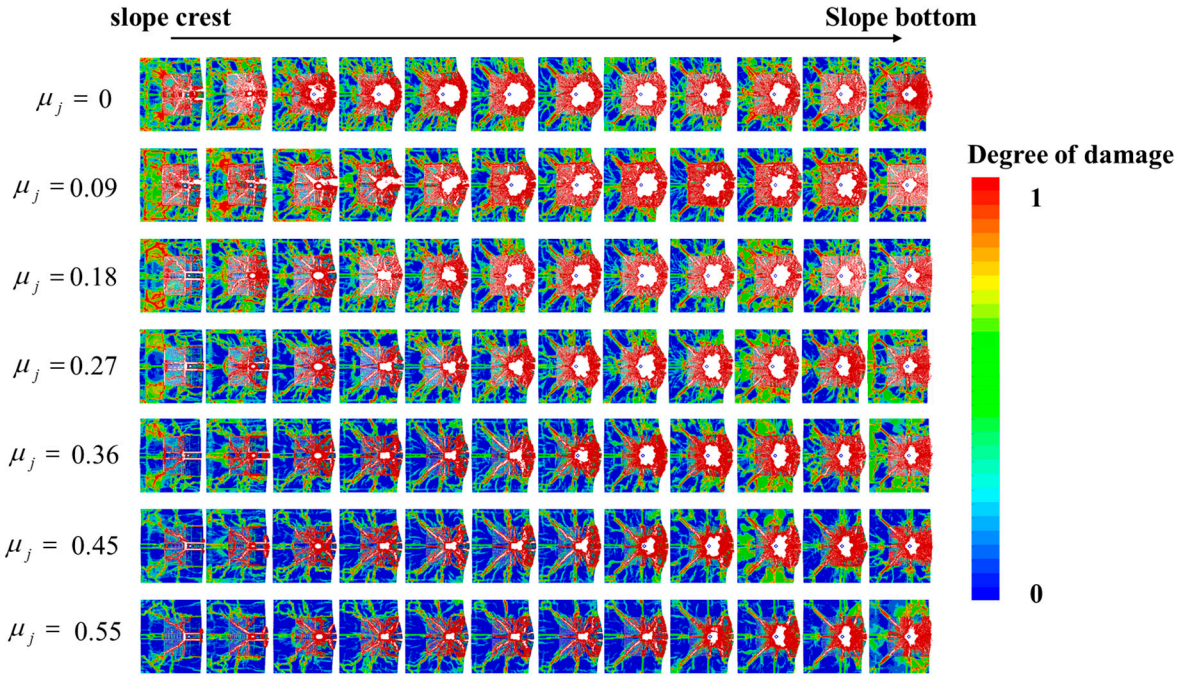

Figure 8: Cross sectional damage diagram of different air gap lengths.

3.3 Analysis of Velocity Variation on Air Deck Slopes of Different Lengths

For the full column charge, the detonation action was intense. The slope surface velocity in the stemming section (Zone 1) reached 49 m/s, as shown in Fig. 9a. In the upper part of the charge section with the small burden (Zone 2), the maximum velocity reached 66 m/s, as shown in Fig. 9b. As the burden

towards the free face increased, the velocity gradually decreased near the slope toe. At the location with the maximum burden at the slope toe, the velocity was approximately 58 m/s, as shown in Fig. 9.

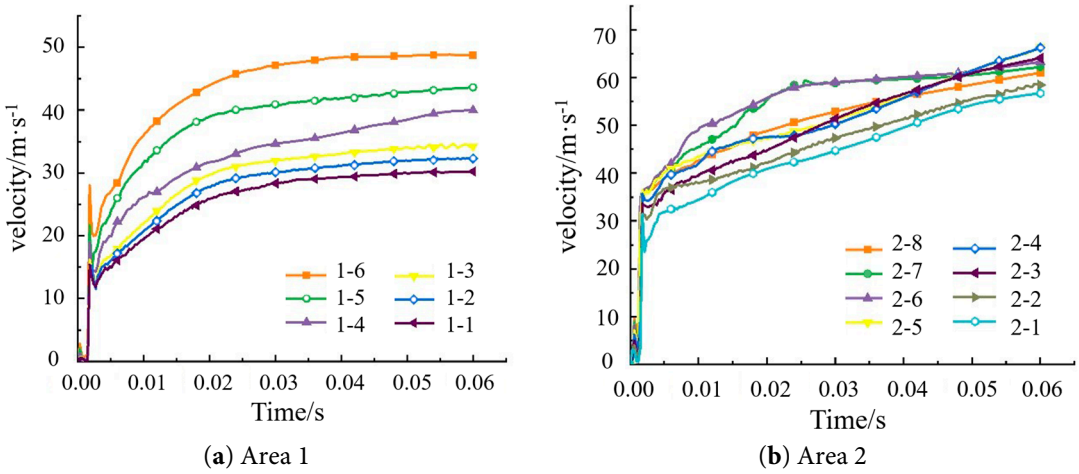

(**a**) Area 1 (**b**) Area 2

Figure 9: Velocity map of slope surfaces for (**a**) Zones 1and (**b**) 2 under full column charge.

The detonation velocity of the full column charge is very fast, typically between 6 to 8 ms, followed by the action of the gaseous products of detonation (GPD) promoting crack propagation and driving the fragmented rock throw. As seen from Fig. 10, the action in deep-hole bench blasting can be divided into two stages. First, the detonation generates a shock wave, inducing a stress wave in the bench rock that propagates to the slope free face. Since stress wave propagation and attenuation occur rapidly, the monitored slope surface velocity exhibits a decay phenomenon. Subsequently, due to the slower gas-driven velocity, the rock velocity in the bench increases slowly, which is more pronounced at the slope crest, as shown in Fig. 10.

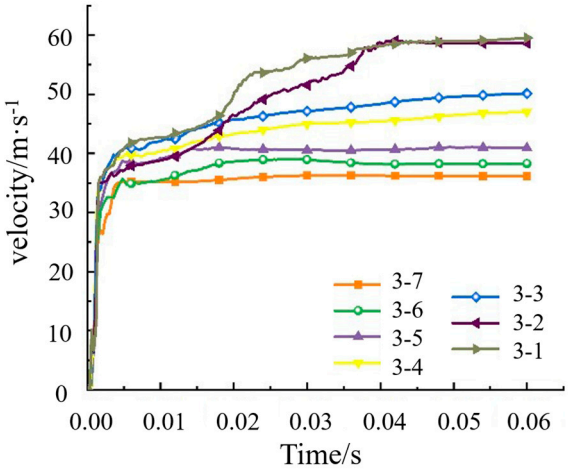

Figure 10: Velocity map of slope surface for Zone 3 under full column charge.

As the air deck length ratio continuously increased, as shown in Fig. 11, the rock movement velocity on the slope surface in the upper stemming area (Zone 1) decreased. When the length ratio was 0.18, the maximum velocity in Zone 1 was 35 m/s, representing a 23.9% reduction compared to the ratio 0.09. At a length ratio of 0.27, the reduction was 39.1% compared to 0.09. When the length ratio increased further, the velocity reduction became less significant, as shown in Fig. 11.

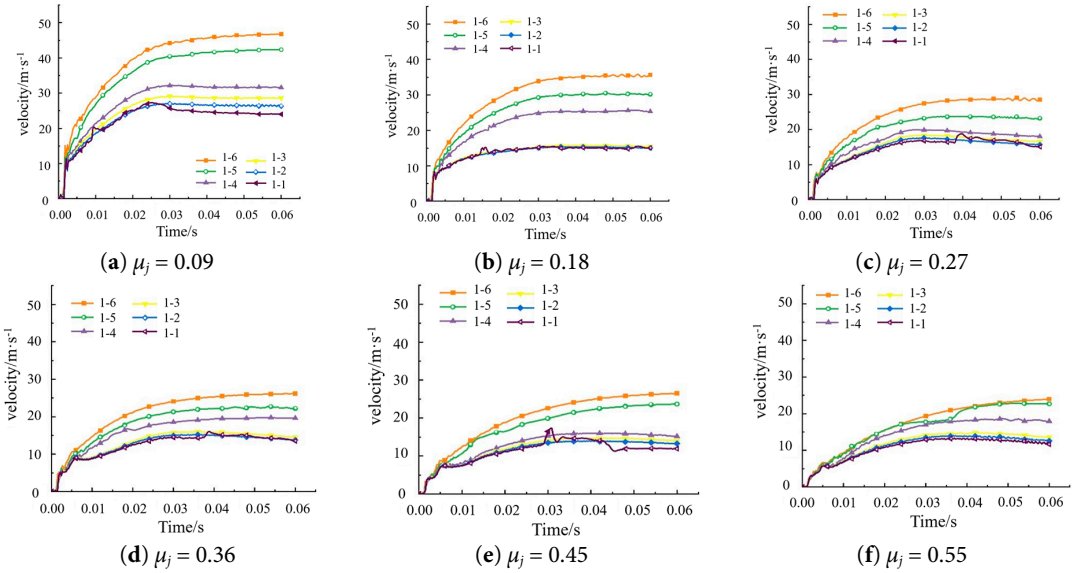

Figure 11: Velocity diagram for Zone 1 with different air deck length ratios (**a**–**f**).

Since stress wave propagation and attenuation occur rapidly, while gas-driven velocity is slower, increasing the air deck length ratio gradually reduced the stress wave action duration but increased the GPD action duration. This indicates that the air deck charge structure effectively improves explosive energy utilization efficiency and increases the action duration. At a length ratio of 0.09, the peak velocity was reached at 25 ms, whereas at 0.18, it was reached at 35 ms. Compared to the full column charge, the GPD action duration was extended by up to 40%. When the length ratio was less than 0.36, the GPD action duration continued to rise within the finite calculation time.

Zone 2 corresponds to the upper charged section of the bench slope. The staged action characteristics of the air deck charge structure are more evident here. As the air deck length ratio increased, the gas-driven action became more pronounced, as shown in Fig. 12a–d. The peak velocity induced by the stress wave acting on the rock movement decreased from 39 m/s to 31 m/s. Compared to the full column charge, the fluctuation was within 10%. Conversely, the gas-driven velocity decreased from 61 m/s to 47 m/s, a reduction of 49.2%. As shown in Fig. 12e,f, with further increase in air deck length ratio, the slope surface rock movement velocity under stress wave action decayed rapidly. The decay rate under stress wave action was greater than that under GPD action, highlighting the significant role of the GPD.

Zone 3 corresponds to the bottom charged section of the bench, where the burden is larger than in conventional bench blasting. Enhancing explosive utilization efficiency and increasing GPD action is particularly important here. The top air deck structure had little influence on the stress wave action from the explosive column at the bench bottom. Only excessively large air deck length ratios reduced the rock movement velocity induced by stress wave action at the bottom, as shown in Fig. 13e,f. Due to the presence of the air deck, the GPD action duration increased. After reverse initiation, the GPD expanded over a longer distance at lower velocity within the air deck section, taking more time to reach the stemming at the top of the hole. After reflection from the stemming, the time for the downward movement increased. Consequently, besides stress wave action and direct GPD action, the secondary action of the reflected GPD from the top was also significant in Zone 3, as shown in Fig. 13a–d. Larger air deck length ratios resulted in longer times for the reflected wave from the stemming to reach the hole bottom.

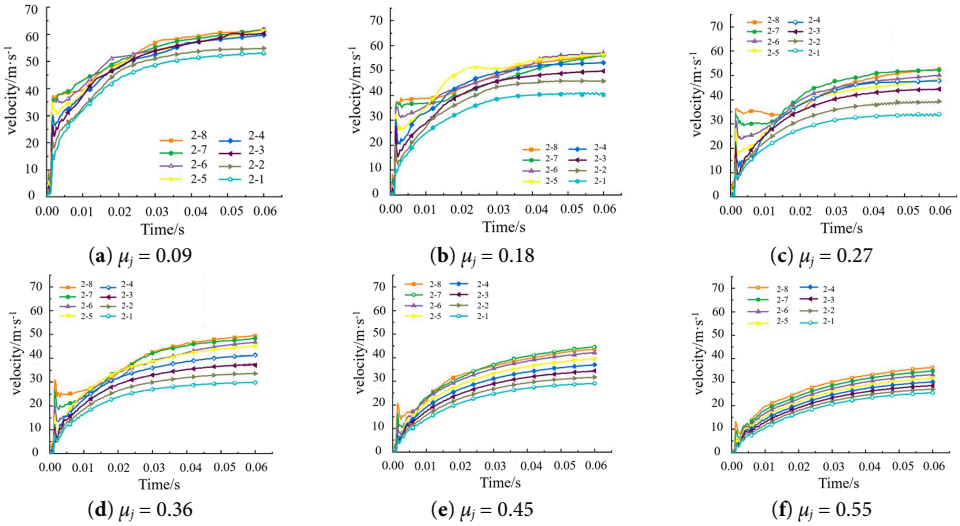

Figure 12: Velocity diagram for Zone 2 with different air deck length ratios (**a**–**f**).

In summary, the shock wave generated by the detonation of the air deck charge induces a stress wave in the bench rock that propagates to the slope surface. Due to the rapid propagation and attenuation of the stress wave, the monitored slope surface velocity exhibits a decay phenomenon. This is followed by gas-driven action; since gas-driven velocity is slower, the rock movement velocity in the bench increases gradually. As the air deck length ratio continuously increased, the slope surface rock movement velocity in the upper stemming area (Zone 1) decreased. For the upper charged section of the bench slope (Zone 2), the staged action characteristics of the air deck charge structure were more evident. In Zone 3, besides stress wave action and direct GPD action, the secondary action of the reflected GPD from the top was also significant.

As shown in Fig. 14, from the full column charge to a length ratio of about 0.37, the slope surface rock movement velocity in the upper-middle Zones 1 and 2 was significant. Within the range of length ratios from 0.27 to 0.55, the velocity reduction in Zone 3 (the bench bottom) was pronounced. The air deck charge structure effectively improves explosive energy utilization efficiency and substantially increases the action duration.

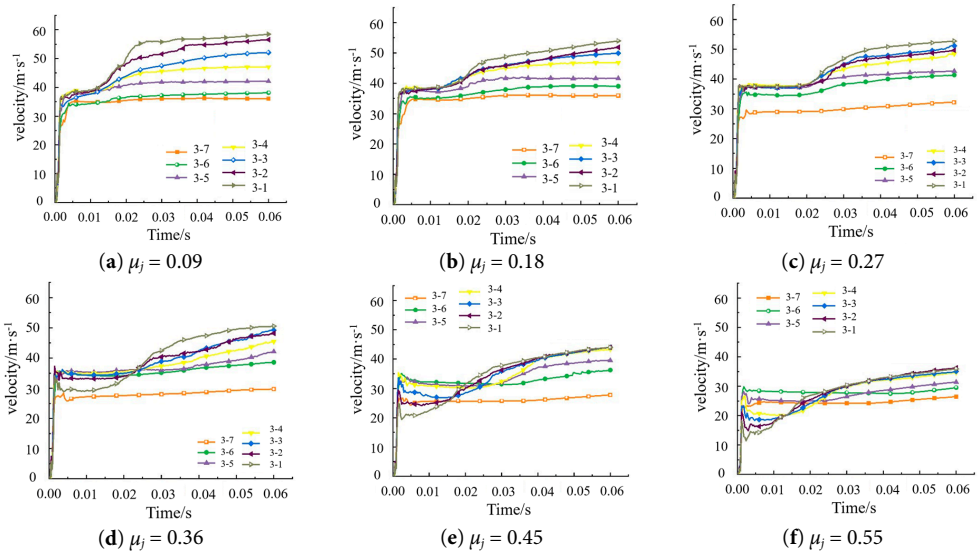

Figure 13: Velocity diagram for Zone 3 with different air deck length ratios (**a**–**f**).

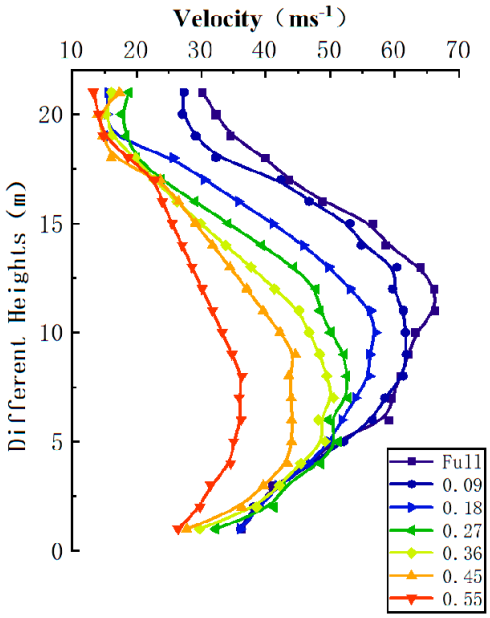

Figure 14: Slope surface velocity diagram for different air deck length ratios.

4 Field Test Results

4.1 High-Speed Photography Observation of Slope Rock Movement

The blasting process with an air deck charge is extremely complex. The detonation of the in-hole explosive and the flow of gaseous products are invisible. The influence of the air deck structure on the in-hole detonation pressure cannot be accurately measured, and conducting tests during large-scale production operations on-site is particularly challenging. High-resolution high-speed photography observation equipment can be used to observe and analyze the bench blasting process. This allows for the detection of microsecond-level state differences under vertical hole air deck charge conditions, such as rock bulge movement on the bench slope, venting of GPD, and rock throw movement flying away from the slope surface. Based on prior theoretical analysis and numerical simulation studies, this method explores the effect of the air deck charge on prolonging the explosive load duration and the rock's dynamic response to reduced in-hole detonation pressure.

The observation employed a Phantom V25001 high-speed camera with a frame rate of 1200 fps (one frame every 0.833 ms), a lens focal length of 200 mm, mounted at a height of 1.5 m, and a resolution of 1280 × 800 pixels. The north direction was defined as the X-axis, east as the Y-axis, and positive elevation as the Z-axis, as shown in Figs. 15 and 16. The straight-line shooting distance was approximately 150 m, outside the warning perimeter.

To facilitate later image processing for correcting the initiation time and hole delay times, a surface observation point needed to be set at the initiation point. This point had the same delay time as the in-hole charge, enabling time monitoring. The purpose was to generate a visible flash point within the camera's field of view at the moment of initiation, serving as a time reference. This avoids the influence of increased explosive detonation time due to longer vertical hole charge lengths. Typically, detonating cord or a primer charge is used, connected to the blast network and placed on the rock surface without obstructing observation. Within the shot image, a "+" shaped crosshair made from two 1 m-long PVC pipes was fixed on the slope surface of the rock mass to be blasted at the observation hole. A static shot before initiation served as the scale reference for the high-speed photography.

Figure 15: Location of the shooting point.

Figure 16: High-speed photography focusing image.

4.2 Observation and Analysis of Blasting Effects with Optimized Charge Structure

For this test, 6 holes with air deck charges in 310 mm diameter vertical holes were selected. By processing the collected images, the image numbers corresponding to the moment GPD venting caused ground uplift and the moment of surface detonator initiation were obtained. The GPD action time inside the hole was calculated by subtracting these two image numbers, multiplying by the time interval per image, and then subtracting the in-hole delay time, as shown in Fig. 17.

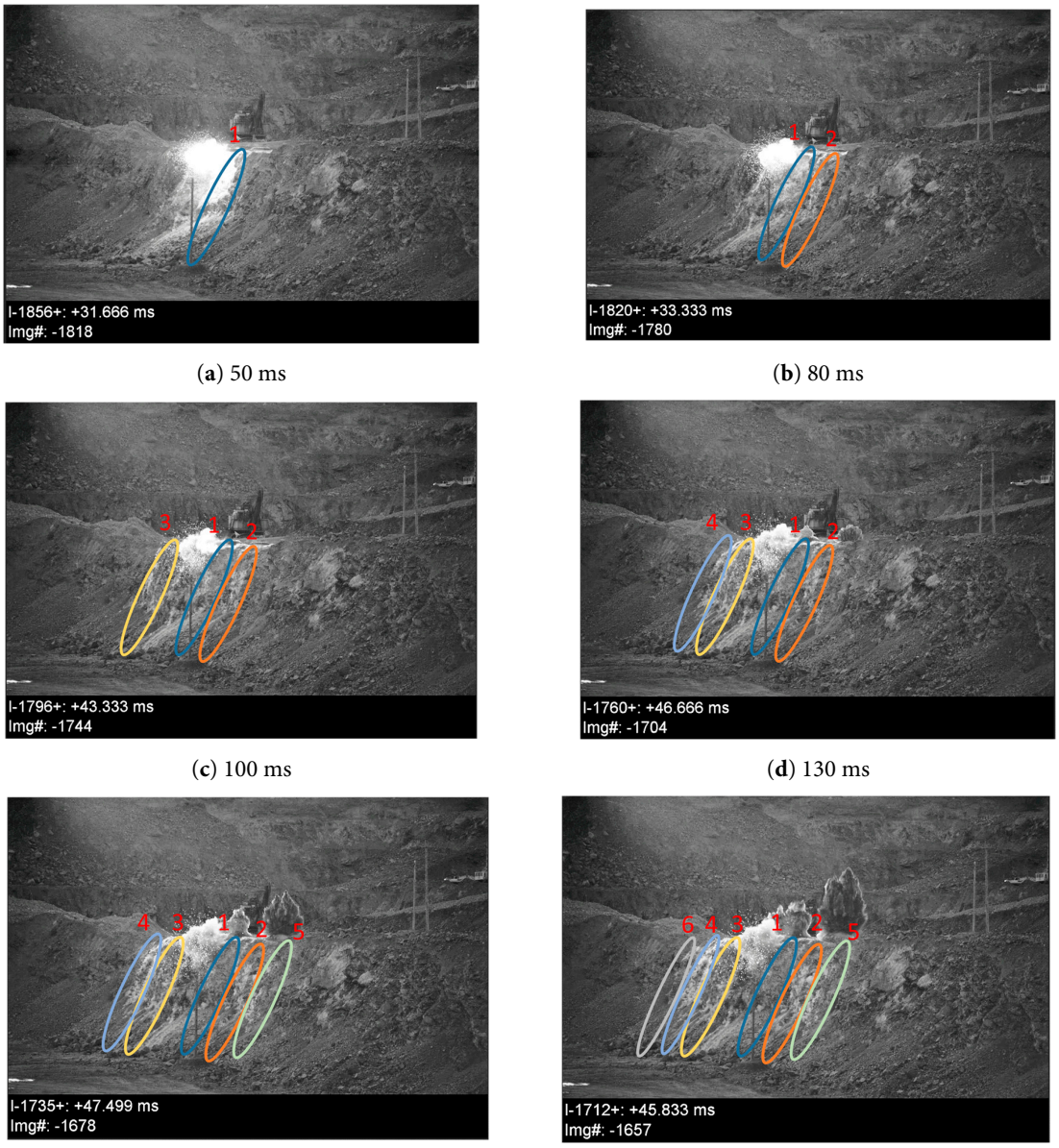

(**a**) 50 ms (**b**) 80 ms

(**c**) 100 ms (**d**) 130 ms

(**e**) 150 ms (**f**) 170 ms

Figure 17: Action time in the vertical hole air deck loading hole (**a**–**f**).

Statistical results are detailed in Table 2.

Table 2: Statistics of action time of explosives loaded in the air deck of the North Side.

Serial Numbers	Delay Time (ms)	Air Deck Position	Air Deck Length m	In-Hole Action Time ms
1	50	0.90	2.15	31.67
2	80	0.85	3.15	33.33
3	100	0.80	4.15	43.33
4	130	0.75	5.15	46.64
5	150	0.73	5.67	47.50
6	170	0.64	7.56	45.83

Analysis showed that for 310 mm large-diameter blastholes, with an air deck length of 2.15 m, the average GPD action time was 31.67 ms. When increased to 4.15 m, the GPD action time reached 43.33 ms. The influence of different air deck positions on the in-hole action time aligned with simulation results. After GPD venting, a bulge formed on the slope surface, rocks flew away from the slope, and were finally thrown and landed. The rock movement process is shown in Fig. 18.

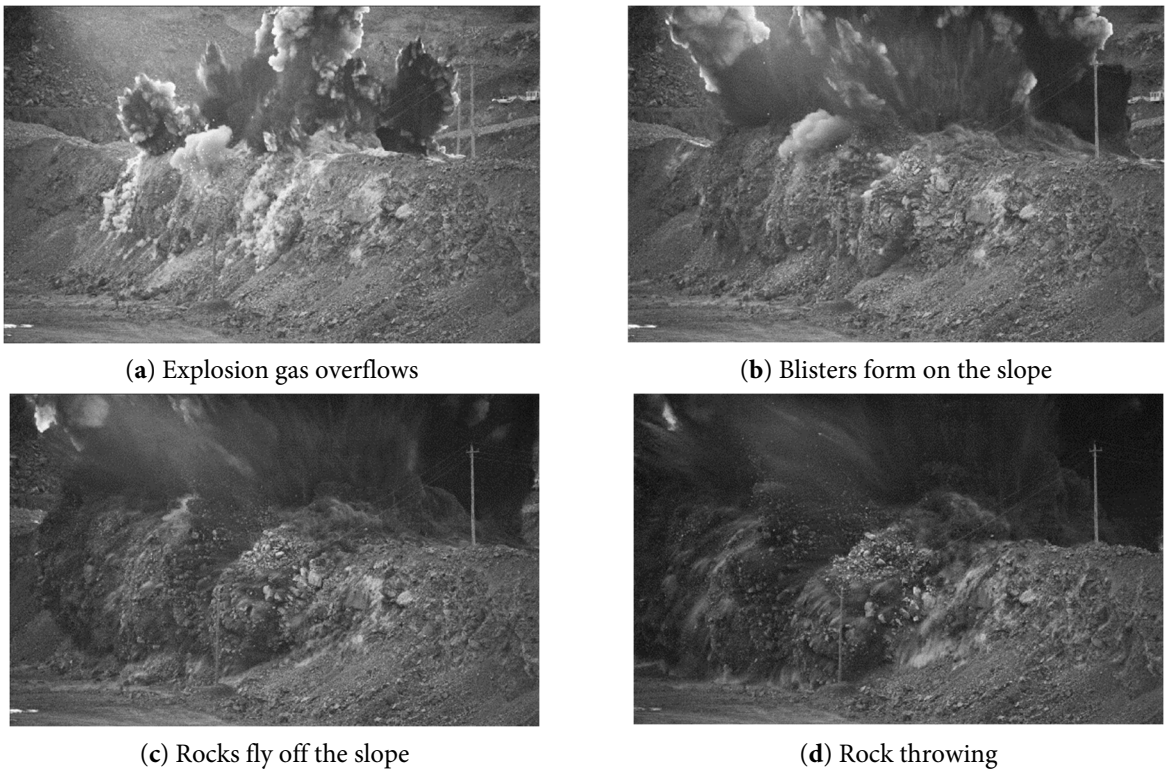

(**a**) Explosion gas overflows (**b**) Blisters form on the slope

(**c**) Rocks fly off the slope (**d**) Rock throwing

Figure 18: Picture of the movement of the flux-loaded rock in the North Side air deck (**a**–**d**).

The air deck charge significantly reduced the in-hole pressure, decreased the initial velocity of rocks flying away from the slope, and mitigated fly rock hazards. The rock flight trajectory is shown in Fig. 19.

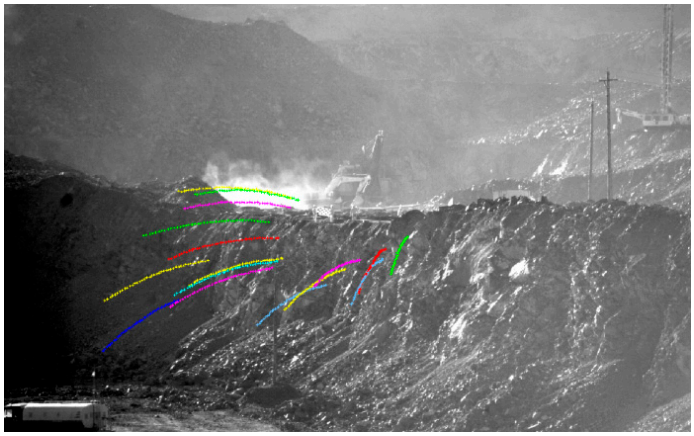

Figure 19: Flight trajectory of rocks in the air deck charge section.

The high-speed camera could observe the state of stemming ejecting from the hole and subsequent moments. PCC professional software was used to analyze and track the velocity of fly rocks at various times. Furthermore, processing and analysis of the collected data showed the average fly rock velocity V = 24 m/s. For the left hole with an 80 ms delay, the upper charge section had a smaller burden, resulting in the highest velocity reaching 33 m/s. This verified the accuracy of the numerical simulation results. The maximum monitored fly rock flight distance was 149 m, less than the mine's stipulated safety distance of 200 m.

5 Conclusions

This study integrated a coupled PBM-FEM-SPH numerical framework with high-speed photographic monitoring and field verification to evaluate the influence of top-air-decked charges on rock fragmentation and kinematic evolution in vertical deep-hole blasting. By establishing selection criteria for optimal air-deck configurations, this research provides a technical foundation for high-density deep-hole blasting operations. The primary conclusions are as follows:

(1) Kinematic Response and Optimal Air-Deck Ratio: Numerical and experimental results indicate that air-decking significantly alters the temporal evolution of rock movement. At low air-deck ratios, the rock mass at the bench crest—characterized by a reduced burden—reaches its peak ejection velocity within 25 ms. Increasing the air-deck length ratio (λ) to 0.27 delays the peak velocity to 45 ms. This shift effectively moderates the rock-throw effect while maintaining the energy required for fragmentation. Consequently, for deep-hole bench blasting and medium-hard rock, a top air-deck length ratio between 27% and 36% is recommended to balance fragmentation quality with hazard suppression.

(2) Influence on Gas Action Duration: Field tests conducted in large-diameter (310 mm) blastholes demonstrate that the air-deck configuration serves as a pressure regulator. An air-deck length of 2.15 m resulted in an average action duration of 31.67 ms for the gaseous products of detonation (GPD). Extending the air-deck length to 4.15 m further increased this duration to 43.33 ms, indicating that larger air gaps facilitate more sustained quasi-static pressure application on the borehole walls.

(3) Fly rock Mitigation and Safety Validation: The application of top-air-decked charges at the bench crest effectively reduces peak detonation pressures while extending the gas expansion phase. This mechanism significantly attenuates the initial ejection velocity of fragments from the slope surface. Field monitoring recorded an average fly rock velocity of 24 m/s (maximum 33 m/s), resulting in a maximum flight distance of 149 m. This distance is well within the site's 200 m safety radius, confirming the effectiveness of air-decked structures in mitigating adverse environmental effects and enhancing the safety of open-pit mining operations.

Acknowledgement: None.

Funding Statement: This research was funded the Key Laboratory of Ministry of Education of China for Efficient Mining and Safety of Metal Mines (No.: ustbmslab202403).

Author Contributions: Zuoming Yin: Conceptualization, Methodology, Investigation, Formal analysis, Writing original draft. Qiang Zhao: Conceptualization, Supervision, Project administration, Writing review & editing, Funding acquisition. Feng Xie: Methodology, Validation, Investigation. Jingjiu Bi: Software, Data curation, Visualization. Jianlong Wang: Resources, Investigation, Validation. Shupeng Zhang: Formal analysis, Writing review & editing. Haonan Wang: Investigation, Data curation. Xiaolong Li: Software, Visualization, Validation. All authors reviewed and approved the final version of the manuscript.

Availability of Data and Materials: All data supporting the findings of this study are included within the paper.

Ethics Approval: Not applicable.

Conflicts of Interest: The authors declare no conflicts of interest.

References

1. Andrievsky AP, Akhpashev BA. Improvement of rock fragmentation by distributed charge blasting. J Min Sci. 2017;53(2):253–8. [CrossRef].
2. Saadatmand Hashemi A, Katsabanis P. The effect of stress wave interaction and delay timing on blast-induced rock damage and fragmentation. Rock Mech Rock Eng. 2020;53(5):2327–46. [CrossRef].
3. Cheng R, Zhou Z, Chen W, Hao H. Effects of axial air deck on blast-induced ground vibration. Rock Mech Rock Eng. 2022;55(2):1037–53. [CrossRef].
4. Costamagna E, Oggeri C, Segarra P, Castedo R, Navarro J. Assessment of contour profile quality in D&B tunnelling. Tunn Undergr Space Technol. 2018;75:67–80. [CrossRef].
5. Gao F, Tang L, Yang C, Yang P, Xiong X, Wang W. Blasting-induced rock damage control in a soft broken roadway excavation using an air deck at the blasthole bottom. Bull Eng Geol Environ. 2023;82(3):97. [CrossRef].
6. Gu W, Wang Z, Chen J, Liu J, Lu M. Experimental and theoretical study on influence of different charging structures on blasting vibration energy. Shock Vib. 2015;2015:248739. [CrossRef].
7. Lou X, Wang Z, Chen B, Yu J. Theoretical calculation and experimental analysis on initial shock pressure of borehole wall under axial decoupled charge. Shock Vib. 2018;2018:7036726. [CrossRef].
8. Lou X, Zhou P, Yu J, Sun M. Analysis on the impact pressure on blast hole wall with radial air-decked charge based on shock tube theory. Soil Dyn Earthq Eng. 2020;128:105905. [CrossRef].
9. Yin Z, Wang D, Wang X, Dang Z, Li W. Optimization and application of spacing parameter for loosening blasting with 24-m-high bench in barun open-pit mine. Shock Vib. 2021;2021:6670276. [CrossRef].
10. Gao J, Zhang L. Evolutionary game analysis of behavioral strategies between government agencies and coal companies—air interval charge blasting technology promotion. Energy. 2025;314:134236. [CrossRef].
11. Li Q, Wei X, Li X, Liu K, Dong L, Tao M, et al. Measurement and stress response analysis of complete history of blast-induced wall pressure for boreholes: a case with air-deck charge. Rock Mech Rock Eng. 2024;57(11):9429–43. [CrossRef].
12. Fang SZ, Li WY, Yang Y, Chen C, Xu P. Experimental study on the dynamic mechanical behavior and energy dissipation characteristics of deep rock under coupled impact loading and hydrostatic pre-stress. J Vib Shock. 2023;42(6):280–8. (In Chinese).
13. Ding C, Yang R, Lei Z, Wang M, Zhao Y, Lin H. Fractal damage and crack propagation in decoupled charge blasting. Soil Dyn Earthq Eng. 2021;141:106503. [CrossRef].
14. Zuo J, Yang R, Gong M, Ma X, Wang Y. Fracture characteristics of iron ore under uncoupled blast loading. Int J Min Sci Technol. 2022;32(4):657–67. [CrossRef].
15. Ding C, Yang R, Chen C, Zhu X, Feng C, Xie Q. Space-time effect of blasting stress wave and blasting gas on rock fracture based on a cavity charge structure. Int J Rock Mech Min Sci. 2022;160:105238. [CrossRef].
16. Zhu HB, Lu WB, Wu L. Research on the mechanism of air interval charging blasting. Rock Soil Mech. 2007;28(5):986–90. (In Chinese).
17. Wang Q, Xiang J, Yue P, Zhang S, Lu Y, Zhang R, et al. Flyrock distance prediction using a hybrid LightGBM ensemble learning and two nature-based metaheuristic algorithms. J Rock Mech Geotech Eng. 2026;18(1):129–50. [CrossRef].
18. Han H, Fukuda D, Liu H, Salmi EF, Sellers E, Liu T, et al. Combined finite-discrete element modelling of rock fracture and fragmentation induced by contour blasting during tunnelling with high horizontal *in-situ* stress. Int J Rock Mech Min Sci. 2020;127:104214. [CrossRef].
19. Mitelman A, Elmo D. Modelling of blast-induced damage in tunnels using a hybrid finite-discrete numerical approach. J Rock Mech Geotech Eng. 2014;6(6):565–73. [CrossRef].
20. Shahrin MI, Abdullah RA, Jeon S, Jeon B, Sa'ari R. Numerical simulation of rock fragmentation by blasting using Discrete Element Method and Particle Blast Method. IOP Conf Ser Mater Sci Eng. 2019;527(1):012032. [CrossRef].

21. Fakhimi A, Lanari M. DEM–SPH simulation of rock blasting. Comput Geotech. 2014;55:158–64. [CrossRef].
22. Petit HA, de Oliveira ALR, Tavares LM. Validation of a rheology-dependent PBM-DEM-CFD simulation model of a continuous vertical stirred mill operating under different conditions. Chem Eng Sci. 2025;306:121260. [CrossRef].
23. Li B, Li Q. Coupled FEM-DEM modeling of permeability evolution in rough fractured shale during shearing under varying confining pressures. J Rock Mech Geotech Eng. 2026;18(3):1736–54. [CrossRef].